Electrode-induced self-healed monolayer MoS_2 for high performance transistors and phototransistors

Sangyeon Pak, Seunghun Jang, Taehun Kim, Jungmoon Lim, Jae Seok Hwang, Yuljae Cho, Hyunju Chang, A-Rang Jang, Kyung-Ho Park, John Hong,* SeungNam Cha*

Dr. S. Pak, T. Kim, J. Lim, Prof. S. Cha
Department of Physics, Sungkyunkwan University (SKKU), Suwon, Gyeonggi-do 16419, Republic of Korea
Email: chasn@skku.edu

Dr. S. Jang, Dr. H. Chang
Chemical Data-Driven Research Center, Korea Research Institute of Chemical Technology (KRICT), Gajeong-ro 141, Daejeon, 34114 Republic of Korea

J. Hwang, Dr. K.-H Park
Nanodevices Laboratory, Korea Advanced Nano Fab Center (KANC), Suwon 16229, Republic of Korea

Prof. Y. Cho
University of Michigan, Shanghai Jiao Tong University Joint Institute, Shanghai Jiao Tong University, Minhang District, Shanghai 200240, P.R. China

Prof. A.-R. Jang
Department of Electrical Engineering, Semyung University, Chungcheongbuk-do 27136, Republic of Korea

Prof. J. Hong
School of Materials Science and Engineering, Kookmin University, Seoul, 02707, Republic of Korea
Email: johnhong@kookmin.ac.kr

Keywords: self-healing, MoS_2, low subthreshold swing, high mobility transistor, ultrasensitive photodetection, flexible photodetector

Abstract

Contact engineering for monolayered transition metal dichalcogenides (TMDCs) is considered to be of fundamental challenges for realizing high-performance TMDCs-based electronic and optoelectronic devices. Here, we establish an innovative concept for a device configuration with metallic copper monosulfide (CuS) electrodes that induces sulfur vacancy healing in the monolayer MoS_2 channel. Excess sulfur adatoms from the metallic CuS electrodes are donated to heal sulfur vacancy defects in MoS_2 that surprisingly improve the overall performance of its transistors and phototransistors. The electrode-induced self-healing mechanism is demonstrated and analyzed systematically using various spectroscopic analyses, DFT calculations, and electrical measurements. Without any passivation layers, the self-healed MoS_2 (photo)transistor with the CuS contact electrodes showed outstanding room temperature field-effect mobility of 97.6 cm^2/Vs, On/Off ratio $>10^8$, low subthreshold swing of 120 mV/decade, high photoresponsivity of 1 x 10^4 A/W and detectivity of 10^{13} jones, which are the best among back-gated transistors that employ CVD-grown 1L MoS_2. Using ultrathin and flexible 2D CuS and MoS_2, we also demonstrated mechanically flexible photosensor, which showed excellent durability under applied bending strain. Our findings demonstrate a promising strategy in TMDCs or other 2D material for the development of high performance and functional devices including self-healable sulfide electrodes.

Monolayered transition metal dichalcogenides (TMDCs) have great potential in developing next-generation flexible, transparent, and wearable electronics and optoelectronics due to their reduced dimensions that offer flexibility and transparency with proper band gap, high carrier mobility, and highly efficient light absorption.[1-3] In addition, their ideally dangling-bond-free surface and atomic thickness are promising for ideal heterogeneous contact and reduced short channel effect,[4] thus making them suitable for future nano-scaled electronic and optoelectronic devices. An ideal field-effect transistor based on a MoS_2 channel is theoretically predicted to reach large on/off ratio ($>10^9$), room temperature mobility of 410 cm^2/Vs, and near-ideal subthreshold swing of 60 meV/decade.[5,6] However, most of experimental results significantly differ from the aforementioned theoretical predictions. One of dominant factors degrading the overall performance of two-dimensional (2D) materials-based devices arises from unwanted chemical interactions between deposited metal electrodes and 2D TMDC channel. These chemical interactions originate from incomplete/imperfect covalent/surface bonds of TMDCs and unwanted damages from the direct deposition of metal layers and precursors, which are used during the device fabrication processes. These lead to the creation of unfavorable interface states and pinning of fermi energy levels, which increase the contact energy barriers and contact resistances, hence impacting the overall electronic and optoelectronic device performance of 2D TMDCs-based devices. Thus, it has been desired to find appropriate contact materials and device fabrication methods that can improve the interface properties between 2D TMDCs and electrode materials.

In this regard, various device fabrication strategies have been proposed to realize clean and atomically sharp metal-TMDC interface properties such as insertion of graphene or hexagonal boron nitride layers,[7] dry transferring of metal layers,[8] assembly of

substitutionally doped TMDCs,[9] employment of indium contacts[10] and phase engineered MoS$_2$.[11] In each case, fabrication processes led to mitigate the partial Fermi level pinning effects and lowered the nontrivial Schottky contact barriers. Nevertheless, such processes require an additional fabrication steps that are difficult to control and/or lead to unwanted chemical interactions that could possibly change inherent characteristics of the TMDC channel materials. Furthermore, anion defects in monolayered TMDCs are naturally built during its high-temperature synthesis or fabrication/transfer steps, resulting in irregular electrical properties upon the device location of a wafer or material preparation methods. It is thus expected to find new electrode system that can not only induce low contact barriers for efficient charge transport but also produce uniform electronic properties of TMDC monolayers.

In this work, we present an innovative, self-healed electrode system that employ metallic copper monosulfide (CuS) electrodes to fabricate high performance transistors and phototransistors based on a chemical vapor deposition (CVD)-grown MoS$_2$ monolayer. We demonstrate that the excess sulfur adatoms from the CuS electrodes provide electrode-induced sulfur vacancy self-healing (SVSH) and reduce defect sites within the MoS$_2$ channel and the MoS$_2$/CuS interface. Furthermore, the SVSH mechanism was explained through surface energy barrier calculation by density functional theory (DFT) that supports the thermodynamically favorable reactions of sulfur adatoms healing on the sulfur vacancies in the MoS$_2$ channel. Without any passivation layers, the MoS$_2$/CuS electronic device reached room temperature field effect mobility of 97.6 cm^2/Vs, On/Off ratio >10^8, and low subthreshold swing of 120 mV/decade in a back-gated transistor configuration, which are highest among reported values for back-gated transistors with CVD-grown MoS$_2$ monolayers.[1,12-18] In addition, the MoS$_2$/CuS phototransistor showed high photoresponsivity of 1 x 10^4 A/W and detectivity of 10^{13} jones, which is among the highest reported values for

4

MoS$_2$-based photodetectors. We further fabricated the two-terminal flexible photodetector to show excellent durability under applied bending strain due to the ultrathin nature and outstanding flexibility of the CuS electrodes and MoS$_2$ monolayer. These findings and development in new CuS contact electrodes pave a powerful strategy to provide CuS electrode-based future electronics and optoelectronics based on 2D TMDC materials.

Results and Discussions

Conductive and transparent copper sulfide (CuS) nanosheet films were prepared by a facile, one-step sulfurization method of Cu metal films (10 nm) which was deposited using a thermal evaporation technique as shown in the schematics and optical image of **Figure 1**a. Note that the Cu metal films were directly exposed to H$_2$S gas under ambient condition at room temperature to synthesize CuS nanosheet films as we previously reported.[19] Reactive H$_2$S gases adsorb onto Cu surface and donate sulfur ions, and copper corrosion reaction with adsorbed sulfur ions leads to the formation of covellite CuS structure. In spite of the ultrathin thickness of CuS, its electrical properties are known to be as good as indium tin oxide (See **Figure** S1 for electrical data).[19] The synthesized CuS nanosheet films possess covellite structure (JCPDS card No. 78-0877) as confirmed by the XRD analysis (**Figure 1**b). The Raman spectrum of CuS shows distinct Raman vibrational modes at around 263.8 cm^{-1} and 471.3 cm^{-1} which correspond to the lattice Cu-S and S-S stretching of covellite, respectively (**Figure S2**).[19]

The MoS$_2$/CuS transistor was fabricated by transferring the CuS nanosheet films onto the MoS$_2$ monolayer (**Figure 1**c). Polystyrene (PS) films were used to detach the CuS/PS films in deionized (DI) water,[20,21] and the films were dried in air to completely remove water molecules to achieve clean interface between the CuS electrodes and MoS$_2$ monolayers. Then, the PS films were attached onto the substrate that has the MoS$_2$

monolayers. To observe and confirm that the CuS electrodes are well attached onto the monolayers of MoS_2, we first performed Raman and photoluminescence (PL) analysis of the MoS_2/CuS heterostructure. **Figure 1**d shows Raman spectrum of the MoS_2 monolayer (black line) and the MoS_2/CuS heterostructure (red line). The Raman spectra of the vertically stacked heterostructure consists of the distinctive Raman peaks of CuS and MoS_2 layers, implying the formation of the MoS_2/CuS heterostructure. The PL spectra (**Figure 1**e) obtained from the MoS_2 monolayer and the MoS_2/CuS heterostructure shows a distinctive emission peak at the characteristic direct exitonic energy at 1.88 eV ($\lambda \sim 660$ nm). Also, it is noticed that there was a significant reduction in the PL intensity for the MoS_2/CuS heterostructure. The reduced PL intensity can be attributed to the exciton dissociation (**Figure 1**f) and charge transfer associated with the formation of metal (CuS)-semiconductor (MoS_2) junction.

The CuS electrode induced SVSH of MoS_2 channel was achieved through mild thermal annealing at 150 ˚C in a vacuum chamber as depicted in **Figure 2**a. Note that only sulfur adatoms are involved during this process, and unreacted H_2S gas does not present within the surface of CuS crystal. The SVSH mechanism is that the excess sulfur adatoms from the CuS electrodes (TEM-EDS spectrum can be found in **Figure** S3) are diffused through the MoS_2 channel and its defect sites (e.g. sulfur vacancies) are healed spontaneously by thermodynamically favorable adsorption/binding of the sulfur adatoms.[22,23] Note that vacancy healing have been previously proposed using chemical treatments to enhance the PL intensity in monolayered TMDCs.[24-26] However, the proposed mechanism was sorely focused on the monolayers themselves and chemical treatments, and the self-healing using device electrodes is not yet explored. To confirm analytically the SVSH mechanism, we first employed XPS analysis as shown in **Figure 2**b. The XPS spectra shows Mo 3d orbital (Mo^{+4} $3d_{5/2}$ and Mo^{+4} $3d_{3/2}$) of the as-grown MoS_2 and the MoS_2/CuS heterostructure. The

deconvoluted peaks can be assigned to intrinsic MoS_2 (i-MoS_2, 230.08 eV and 233.23 eV) and defective MoS_2 (d-MoS_2, 229.83 eV and 232.98 eV).[22,27] When the as-grown MoS_2 monolayer is healed by the sulfur adatoms from the CuS electrodes, the peak contribution from the i-MoS_2 is increased, whereas the d-MoS_2 is decreased, resulting in the shift of the doublets to the higher binding energy. The XPS spectra of S 2p also confirms the SVSH mechanism (**Figure** S4).[22,28]

The SVSH mechanism was also confirmed using annular dark field scanning tunneling electron microscope (ADF-STEM) measurement, and the direct vision of the atomic structure were obtained for pristine MoS_2 and MoS_2/CuS heterostructure as shown in **Figure** 2c and d, respectively. The STEM images of the pristine MoS_2 crystals clearly showed the spatial distribution of the Mo and S atoms, and the Mo atoms appear brighter than the S atoms. As shown in **Figure** 2c, the vacancy sites of S atoms in pristine MoS_2 are darker than the Mo and S atoms. On the contrary, the self-healed MoS_2 (**Figure 2**d) displayed uniform atomic arrangement, which implicates that the SVSH by the CuS electrodes can effectively decrease the sulfur vacancies in the monolayered MoS_2.

To further elucidate the CuS-induced SVSH mechanism and the effect of SVSH, the PL spectrum was obtained from the overlapped CuS/MoS_2 regions (region 1- CuS/MoS_2, region 2 and 3- MoS_2 in the inset image) as shown in **Figure 2**e, and the PL intensity mapping image can be seen in **Figure** S5. The PL intensity of MoS_2 at the region 1 is largely decreased due to the formation of metal-semiconductor junction. On the contrary, at the region 2 and 3, the PL intensity was largely increased. The PL intensities are even higher than that of as-grown monolayered MoS_2. Such changes in the PL intensity are attributed to the CuS-induced vacancy healing, and such healing trends were also confirmed previously, where the PL quantum efficiency of MoS_2 was enhanced due to the reduced number of defect sites and the consequent nonradiative recombination within the MoS_2 crystals.[25,27]

The energy band alignment of the MoS_2 and CuS electrodes before and after the thermal annealing have been further probed by a kelvin probe force microscope (KPFM) to verify the effect of the SVSH on the energy levels of MoS_2. It should be noted that surface/interface defect states are known to affect the energy level offset and alignment between the electrodes and the channel. Reduced sulfur vacancy sites can also lower the contact energy barriers and induce the efficient charge transfer.[29,30] The 2D work function mapping at the CuS/MoS_2 heterostructure was obtained before and after the thermal annealing process (**Figure 2**f,g). The KPFM images represent the noticeable band offset between the MoS_2 and CuS electrodes junction before the annealing process, while the difference in the work function is relatively decreased after the annealing process, as observed by the color difference and small energy depth on the line profiles (**Figure 2**h) which are directly extracted from the KPFM mapping images in **Figure 2**f,g. Also, the work function of CuS and MoS_2 is slightly changed possibly due to the desorption of oxygen/water molecules[31] and/or diffusion of sulfur adatoms from CuS to MoS_2. The work function line profiles clearly show, before the annealing process, a noticeable intrinsic band offset around 60 meV and the corresponding depletion region between the MoS_2 monolayer and CuS electrodes. After the mild thermal annealing, the band offset is relatively reduced as well as the depletion region. The contact energy barriers between the MoS_2 monolayer and CuS electrodes are reduced due to the SVSH mechanism, which is in accordance with the XPS, STEM, and PL results.

To further support our claim that the sulfur adatoms can favorably heal the sulfur vacancies in MoS_2, we calculated the binding energy surfaces (BESs) of sulfur adatoms in different positions over the various (perfect and defective) MoS_2 surfaces by using first-principles calculations (see Experimental Section for details). The BESs were calculated by moving the position of the sulfur adatom on each point of the different MoS_2 surface states as

8

depicted in the lower image of **Figure 3**a. We intentionally modelled the several types of the sulfur vacancies states including a sulfur single vacancy (V_S), two neighboring sulfur single vacancies ($2V_S$), two neighboring sulfur double vacancies ($2V_{S2}$), and V_S with a sulfur adatoms (S_A) (**Figure 3**a,c and **Figure** S6). The binding energy was defined as $E_{bind} = E_{S\text{-}adatom/Surface} - (E_{S\text{-}adatom} + E_{Surface})$, where $E_{S\text{-}adatom/Surface}$ is the total energy of the total system that the sulfur adatom is adsorbed on the particularly modelled surface, and $E_{S\text{-}adatom}$ and $E_{Surface}$ are the total energies of the isolated S atom and modelled surface (Perfect and defective MoS_2 surfaces), respectively. For the perfect MoS_2 surface, the color map distribution of the BES of the sulfur adatoms correspond to the atomic arrangement of Mo-top (MT), S-top (ST) and hollow (H) sites (upper, **Figure 3**a), which are in good agreement with the atomic geometry of MoS_2. When sulfur vacancies are introduced, noticeable drop (blue puddles) in the binding energy was monitored as clearly distinguished in color map of **Figure 3**b,c. The binding energy of the sulfur adatom at the sulfur vacancy in MoS_2 is calculated to be around -3.7 eV, regardless of the types of vacancy states, suggesting that the adsorption of sulfur adatoms on the sulfur vacancy sites is thermodynamically spontaneous and favorable. These results are also in good agreement with the previously reported results, in which the excess oxygen adatoms can favorably attached on the sulfur vacancies in MoS_2.[32] It should be also noted that the adsorption energy of sulfur adatoms on the sulfur vacancy sites is much higher than the desorption energy of sulfur adatoms from CuS surface, suggesting that the desorption and diffusion process is likely to happen energetically under the concentration gradient and mild thermal annealing (**Figure** S7).

Furthermore, the changes in the surface diffusion energy barrier around the sulfur vacancy sites were calculated. **Figure 3d** shows the diffusion energy barrier profiles extracted from proposed surface diffusion paths (double-headed arrows in a-c, a combination of ST-ST-ST or ST-V_S-ST). In the perfect MoS_2 surface, the calculated diffusion energy

barrier was found to be ~ 1.6 eV along with the diffusion pathway presented in **Figure** 3d. When the sulfur adatom is placed around the sulfur vacancy, the surface diffusion energy barrier on the MoS_2 surface with the sulfur single vacancy ($1V_S$/unit-cell) decreases to ~ 0.9 eV compared to that of the perfect MoS_2 surface. In the case of the MoS_2 surface with the two neighboring sulfur single vacancies ($2V_S$/unit-cell), the reduction of diffusion energy barrier is more volatile (the calculated diffusion energy barrier on 2Vs is 0.4 eV, **Figure** 3e). Additionally, the effect of the diffusion energy barrier on the presence of S2 double vacancies (V_{2S}/unit-cell) or additional sulfur adatom (S_A) was also checked as shown in **Figure** S6. In the both cases, the diffusion energy barrier reaches to the ~0.7 eV and 0.9 eV, which shows the similar reduction behavior (**Figure 3**b,c). Lowering both binding energy surface and diffusion energy barrier within the sulfur vacancy sites confirms that the excess sulfur adatoms from the CuS electrode can favorably diffuse across the surface of MoS_2 as well as bind and heal the sulfur defect sites in MoS_2.

To understand in detail how the SVSH mechanism affects the electrical properties of MoS_2, we have fabricated MoS_2/CuS field effect transistors (FETs) on a HfO_2/Si substrate and the electrical properties of 20 control-devices were carefully examined before and after the thermal annealing process. The schematic picture of the MoS_2/CuS FET is depicted in **Figure 4**a. **Figure 4**b presents the representative drain current as a function of the gate voltage, which is shown in a logarithmic scale at drain voltages of $V_{ds} = 0.1, 0.3, 0.5$ V, and **Figure 4**c shows the drain-source current as a function of the drain-source voltage on a linear scale for the as-fabricated and self-healed MoS_2/CuS FETs. The both as-fabricated and self-healed FETs exhibit the n-type characteristics, steep subthreshold swing, low off currents, high on currents, and ohmic contact as observed in the transfer and output curves, indicating that the CuS electrodes can be well applied for the metal-semiconductor contact and the low electron barrier with the MoS_2 channel. From the transfer characteristics, we estimated a field

10

effect mobility using $\mu_{FE} = \frac{L}{WC_{ox}V_{ds}}\frac{dI_{ds}}{dV_{gs}}$, where L and W are channel length and width, C_{ox} is

the gate capacitance of 309.9 nF cm^{-2}. After the thermal annealing, the room temperature,

back-gated field-effect mobility of MoS$_2$/CuS FET is surprisingly increased from 32 to 97.6

cm^{2}V^{-1}s^{-1}, which demonstrate about the 3-fold improvement in its mobility. Furthermore, the

self-healed MoS$_2$/CuS FET showed noticeable improvement in the On/Off ratio and

subthreshold swing value as shown in **Figure 4**b and d. The On/Off current ratio is increased

from 10^6 to $>10^8$ upon mild thermal annealing. Furthermore, the subthreshold swing values of

the self-healed MoS$_2$/CuS FETs were decreased by 33 % and reached the value as low as 120

mV/decade in a back-gated transistor configuration without any passivation layers. The

improvement in the electrical properties of the self-healed devices can be attributed to the

enhanced contact properties resulting from creation of chemically clean interface and

reduction of unwanted Fermi-level pinning (see **Figure** S8 for contact resistance

measurement). The electrical properties of annealed CuS and MoS$_2$/CuS FET at 300 ˚C

showed similar electrical properties (**Figure** S9). The improvement in the mobility as well as

subthreshold swing is a clear signature of the reduced defects and interface trap densities

within the device channel and the interface.[29,33] Our MoS$_2$/CuS transistor showed impressive

device performance (mobility, on/off ratio, and SS) and the values are the best reported so far

among back-gated transistors with CVD-grown 1L-MoS$_2$, which is compared in **Table** S1.

Furthermore, the electrical properties of our device are significantly better than the device

with copper contact and previously demonstrated vacancy-passivated devices (see **Figure**

S10 and **Table** S2 for comparison).

It is also evident that the threshold voltages were shifted towards positive voltages

for the self-healed devices as shown in **Figure 4**e. At the drain voltage V_{ds} = 0.5 V, the

threshold voltages were significantly changed from -3.4 V to -0.8 V which were determined

using a linear-extrapolation method, and the statistical charts, showing the shift of threshold

11

voltages, are plotted in **Figure** S11. We attribute such change in the threshold voltages to the

SVSH in the MoS_2 channel, which shift fermi energy level toward the intrinsic level. To

further elucidate that the shifts of threshold voltages is due to the SVSH in the MoS_2 channel,

we also measured and compared the hysteresis behaviors of the as-fabricated and self-healed

MoS_2/CuS FETs as shown in **Figure 4**e. A noticeable decrease in the hysteresis width was

observed for the self-healed device compared to the as-fabricated device, which is a signature

of reduced surface adsorbates due to the self-healed MoS_2 channel that are less energetically

active to the adsorbates.[34]

The results presented thus far demonstrate the effect of the SVSH for the field-effect

transistor applications. We now consider phototransistor performance of the self-healed

MoS_2/CuS devices. It should be noted that defects can play as recombination centers during

photodetection and impede efficient charge transport,[35,36] and the self-healed devices are

expected to reach high photoresponsivity due to reduced scattering/recombination during

photogenerated carrier transport/transfer from MoS_2 to CuS electrode. **Figure 5**a shows the

transfer curve of the self-healed MoS_2/CuS phototransistor under various illumination

intensities. The incident laser power density is estimated by considering the laser spot size (a

diameter of 2 mm). Based on the measurement in **Figure 5**a, the photoresponsivity of the

self-healed device is estimated using the equation $R = \frac{I_{Ph}}{P}$, where the I_{Ph} is the photocurrent

and P is the incident laser power on the effective area of the devices. The photoresponsivity

was plotted with respective to the incident laser power with varying gate voltages as shown in

Figure 5b. We found that the photoresponsivity as high as $R = 13461.5$ A/W was calculated

at $V_g = +4$ V and $P = 3.4 \times 10^{-3}$ mW/cm^2. The dependence of photoresponsivity on the

incident laser power follows a power law,[37] $R \approx P^{\alpha}$, where α is ranging from -0.76 to -0.92,

which is higher than the values reported by other 2D based photosensors[37-39] and is close to

the saturation factor $\alpha = -1$. Specifically, the non-unity exponent generally involves defect

12

sites,[35] and the high α value suggests that the MoS_2/CuS phototransistor has less defects by the SVSH.

Figure 5c shows the stable and repeated temporal response of the self-healed device after switching the 450 nm laser illumination on and off for 3 s under applied bias voltages of V_{ds} = 0.1 V and 0.5 V and V_g = 0 V. A fast rise and decay time of 90 ms and 160 ms, respectively, were observed for the MoS_2/CuS device. We further tested the phototransistor performance by measuring and plotting photoresponsivity and specific detectivity, D^*, with respective to the back-gate voltages as shown in **Figure 5**d. The high photoresponsivity under the positive polarity back gate voltages can be attributed to the lower contact resistance which effectively propagate charges into the MoS_2 channel.[40] The D^* was also found to be dependent on the back-gate voltages (see **Figure** S12 for detectivity and NEP calculation).[36,41,42] While R reached the highest value under the positive polarity gate voltage, D^* was increased up to 10^{13} jones under the negative polarity gate voltage due to the significantly reduced dark current, and the values are among the highest reported performance for pristine MoS_2-based photodetectors as summarized in **Table** S3.

The attractive features of the 2D MoS_2 channel and ultrathin CuS electrodes in terms of their outstanding electrical properties and their flexibility enable us to explore new avenues for developing flexible optoelectronics based on those 2D materials. The ultrathin CuS electrode not only induce self-healing in MoS_2, but also possess excellent electrical properties and outstanding stability under mechanical strain, thus making them highly suitable for flexible applications. In order to address the feasibility of our self-healed MoS_2/CuS device in flexible device applications, we have designed and fabricated a simple two-terminal flexible MoS_2 photodetector on a flexible Polyethylene terephthalate (PET) substrate, and the resulting device image is shown in **Figure 6**a. The drain source-current *versus* drain-source voltage under varying illumination intensities is plotted in a logarithmic

13

scale in **Figure 6**b. It can be seen that the flexible MoS_2/CuS device shows the symmetric, ohmic contacts and current modulation under the 450 nm laser illumination. Based on the measured data, the photoresponsivity, *R*, was reached up to 7 A/W when it was calculated with respective to the applied voltages as shown in **Figure 6**c.

To further investigate and characterize the MoS_2/CuS flexible photodetector, we have performed in-situ bending photoresponse measurements as shown in **Figure 6**d. The inset image of **Figure 6**d shows our bespoke bending machine employed to apply strain on the photodetector. Along with the changes in the dark current, the photocurrent was increased as the bending radius decreases down to 3.5 mm. Such trend observed for the flexible MoS_2/CuS photodetector under bending strain is consistent with the previous report showing piezoresistive effect,[43] where the contact barrier height is reduced due to the changes in the electron affinity under the applied tensile strain and the corresponding photo-electrical properties are improved due to the reduced contact barriers.

To investigate mechanical stability of our MoS_2/CuS flexible photodetector, we have monitored the change in the dark current and photocurrent in terms of the number of bending cycles at a bending radius of 4 mm. As shown in **Figure 6**e, the photocurrent and dark current was well maintained with only a slight variation in the magnitude even the device was bent up to 10^4 cycles, and the time domain photocurrent was measured to shown the stability of our MoS_2/CuS flexible photodetector before and after the bending tests as shown in **Figure 6**f. Such high stability of our MoS_2/CuS flexible photodetector under mechanical bending tests is strongly attributed to the ultrathin nature of CuS electrodes as well as high young's modulus of MoS_2 monolayer, all of which are highly suitable for next-generation flexible optoelectronic device applications.

Conclusion

In conclusion, we have developed the innovative self-healed sulfide-electrode system for 2D MoS_2 devices that showed impressive transistor and phototransistor performance. We have shown that mild thermal annealing in the CuS/MoS_2 heterogenous structure induces excess sulfur adatoms to heal the defect sites of MoS_2 monolayer, as known as sulfur vacancy self-healing, which in turn improves contact and MoS_2 channel properties. The self-healed, back-gated transistors and phototransistors showed high mobility up to 97.6 cm^2/Vs, low subthreshold swing of 120 mV/decade, high photoresponsivity up to 13461.5 A/W, and detectivity up to 10^{13} jones without any passivation layers. We further demonstrated the flexible photodetector based on the CuS electrodes and MoS_2 channel and proved the outstanding mechanical stability under the multiple bending test. We believe that our device integration approaches should pave a new way of designing (opto)electronics based on 2D TMDC materials and CuS electrode.

Experimental Section

Synthesis of monolayer MoS_2 and CuS nanosheet: Monolayer MoS_2 was grown on a 300 nm SiO_2/Si substrate using a thermal CVD method and thermodynamically stable synthesis.[44,45] The growth was carried in a 2 inch quartz tube by placing 0.05 mg of MoO_3 precursor (Sigma Aldrich, > 99%) and 50 mg of sulfur powder (Sigma Aldrich, > 99.98%) which was placed upstream of the furnace. The growth was carried at 750 – 800 ˚C for 5 to 10 minutes. CuS nanosheet was synthesized by exposing the Cu film to ammonium sulfide (Alfa Aesar, 20-24% aq. soln.). Cu film was deposited using a thermal evaporator.

Fabrication of MoS$_2$ and CuS nanosheet heterostructure: The electrode pad for the CuS electrodes were patterned using a standard photolithography process. To transfer MoS$_2$ monolayers and CuS electrodes, polystyrene (PS) film was used as the transferring medium.[21] MoS$_2$ and CuS electrodes were spin coated with PS (M$_W$ ~ 192,000) film. During the transfer process, the PS film holds MoS$_2$ and CuS layers, while water penetrates between the PS film and the substrate for detachment. The detached PS film with MoS$_2$ or CuS is dried in air and transferred onto the targeting substrate (SiO$_2$, HfO$_2$, and PET substrate). The PS film was removed by dipping the substrate in toluene for 24 hrs. For the preparation of the XPS sample, large area and fully covered MoS$_2$ film (> 5 mm x 5 mm) was transferred on CuS film (> 5 mm x 5mm) which was synthesized on SiO$_2$/Si substrate. The fabricated MoS$_2$/CuS heterostructure was annealed at 150 ˚C under vacuum condition.

Characterization of MoS$_2$ and CuS: The Raman and PL measurements were carried out using 532 nm laser on Alpha 300 R confocal Raman spectroscopy. KPFM images were obtained using a commercial AFM setup (Park Systems, XE7) with a lock-in amplified (SR-830, Stanford Research Systems). For KPFM measurement, Cr/Au-coated Si tip (NSC14) was used. The tip was calibrated with highly oriented pyrolytic graphite (HOPG) before KPFM measurement.

Electrical and optoelectrical measurement: (opto)electrical properties were measured using the semiconductor characterization system (4200A-SCS, Keithley), Tektronix MDO3054 oscilloscope, Stanford Research Systems SR570 current preamplifier, and MS Tech probe station. Strain-dependent photocurrent measurement was carried out using our bespoke bending machine and bending machine motorized system (ST-BJS-0810-SSU) for the bending cycle tests. 450 nm laser diode (MDL-III-450L) was used to measure the photoresponse of MoS$_2$/CuS devices.

DFT Calculations: The atomic geometries and sulfur adatom binding energies of the various MoS$_2$ surface structures were calculated using the Vienna *ab initio* simulation package (VASP).[46,47] The exchange–correlation functional was approximated using the Perdew–Burke–Ernzerhof (PBE) expression.[48] In order to account for weak van der Waals (vdW) interactions between sulfur adatom and MoS$_2$ surfaces, the optB86b-vdW functional, implemented in VASP by Klimeš et al., was used for all of the binding energy calculations.[49] Electron–ion interactions were modeled using the projector augmented wave (PAW) method.[50] The electronic wave functions were expanded in a basis set of plane waves with a kinetic energy cutoff of 500 eV. The geometry relaxation step was repeated until the ionic forces were reduced to below 0.01 eV Å^{-1}. The k-space integration step was performed with finite sampling of the k-points on a $6 \times 6 \times 1$ mesh in the Brillouin zone to optimize the geometry of each modeled structure. To minimize the interactions between neighboring image cells, vacuum regions at least 23 Å in length along the direction (z) perpendicular to the 2D surface were included. For the BES calculation of the sulfur adatom, atomic geometry optimizations of five MoS$_2$ model surfaces, specifically those of perfect MoS$_2$ surface and four defective MoS$_2$ surfaces with $1V_S$ or $2V_S$ or $2V_{2S}$ or $1V_S$ & $1S_A$ (per unit-cell), were performed preferentially. All MoS$_2$ model surface systems were fully relaxed. After that, for the relaxed perfect and defective MoS$_2$ surface structures obtained from the prior calculation, the overall molybdenum atoms were fixed during the geometry optimization of the sulfur adatom adsorbed on the various model surfaces to maintain the original structures of the pre-relaxed MoS$_2$ surfaces. Also, the x and y positions of the sulfur adatom were fixed, and only its z position was relaxed.

Acknowledgements

References

[1]   J. Lee, S. Pak, Y.-W. Lee, Y. Cho, J. Hong, P. Giraud, H. S. Shin, S. M. Morris, J. I. Sohn, S. Cha, J. M. Kim, *Nat. Commun.* **2017**, 8, 14734.

[2]   S. Pak, J. Lee, Y.-W. Lee, A.-R. Jang, S. Ahn, K. Y. Ma, Y. Cho, J. Hong, S. Lee, H. Y. Jeong, H. Im, H. S. Shin, S. M. Morris, S. Cha, J. I. Sohn, J. M. Kim, *Nano Lett.* **2017**, 17, 5634.

[3]   S. Pak, A. R. Jang, J. Lee, J. Hong, P. Giraud, S. Lee, Y. Cho, G. H. An, Y. W. Lee, H. S. Shin, S. M. Morris, S. Cha, J. I. Sohn, J. M. Kim, *Nanoscale* **2019**, 11, 4726.

[4]   J. Wang, Q. Yao, C. W. Huang, X. Zou, L. Liao, S. Chen, Z. Fan, K. Zhang, W. Wu, X. Xiao, C. Jiang, W. W. Wu, *Adv. Mater.* **2016**, 28, 8302.

[5]   Y. Yoon, K. Ganapathi, S. Salahuddin, *Nano Lett.* **2011**, 11, 3768.

[6]   K. Kaasbjerg, K. S. Thygesen, K. W. Jacobsen, *Phys. Rev. B* **2012**, 85, 115317.

[7]   Y. Liu, H. Wu, H. C. Cheng, S. Yang, E. B. Zhu, Q. Y. He, M. N. Ding, D. H. Li, J. Guo, N. O. Weiss, Y. Huang, X. F. Duan, *Nano Lett.* **2015**, 15, 3030.

[8]   Y. Liu, J. Guo, E. B. Zhu, L. Liao, S. J. Lee, M. N. Ding, I. Shakir, V. Gambin, Y. Huang, X. F. Duan, *Nature* **2018**, 557, 696.

[9]   H. J. Chuang, B. Chamlagain, M. Koehler, M. M. Perera, J. Q. Yan, D. Mandrus, D. Tomanek, Z. X. Zhou, *Nano Lett.* **2016**, 16, 1896.

[10]   Y. Wang, J. C. Kim, R. J. Wu, J. Martinez, X. J. Song, J. Yang, F. Zhao, K. A. Mkhoyan, H. Y. Jeong, M. Chhowalla, *Nature* **2019**, 568, 70.

[11]   R. Kappera, D. Voiry, S. Yalcin, B. Branch, G. Gupta, A. Mohite, M. Chhowalla, *Nat. Mater.* **2014**, 13, 1128.

[12]   A. M. van der Zande, P. Y. Huang, D. A. Chenet, T. C. Berkelbach, Y. You, G. H. Lee, T. F. Heinz, D. R. Reichman, D. A. Muller, J. C. Hone, *Nat. Mater.* **2013**, 12, 554.

[13]   Y. J. Zhan, Z. Liu, S. Najmaei, P. M. Ajayan, J. Lou, *Small* **2012**, 8, 966.

[14]   W. Park, J. Baik, T. Y. Kim, K. Cho, W. K. Hong, H. J. Shin, T. Lee, *ACS Nano* **2014**, 8, 4961.

[15]   Z. F. Zhang, X. L. Xu, J. Song, Q. G. Gao, S. C. Li, Q. L. Hu, X. F. Li, Y. Q. Wu, *Appl. Phys. Lett.* **2018**, 113, 202103.

[16]   H. Kwon, S. Garg, J. H. Park, Y. Jeong, S. Yu, S. M. Kim, P. Kung, S. Im, *Npj 2d Mater Appl* **2019**, 3, 9.

[17]   T. Y. Kim, M. Amani, G. H. Ahn, Y. Song, A. Javey, S. Chung, T. Lee, *ACS Nano* **2016**, 10, 2819.

[18]   S. Pak, J. Lim, J. Hong, S. Cha, *Catalysts* **2021**, 11, 70.

[19]   J. Hong, B. S. Kim, B. Hou, S. Pak, T. Kim, A. R. Jang, Y. Cho, S. Lee, G. H. An, J. E. Jang, S. M. Morris, J. I. Sohn, S. Cha, *ACS Appl. Mater. Interfaces* **2021**, 13, 4244.

[20]   A. Gurarslan, Y. F. Yu, L. Q. Su, Y. L. Yu, F. Suarez, S. Yao, Y. Zhu, M. Ozturk, Y. Zhang, L. Y. Cao, *ACS Nano* **2014**, 8, 11522.

[21]   S. W. Jung, S. Pak, S. Lee, S. Reimers, S. Mukherjee, P. Dudin, T. K. Kim, M. Cattelan, N. Fox, S. S. Dhesi, C. Cacho, S. Cha, *Appl. Surf. Sci.* **2020**, 532, 147390.

[22]   X. K. Zhang, Q. L. Liao, S. Liu, Z. Kang, Z. Zhang, J. L. Du, F. Li, S. H. Zhang, J. K. Xiao, B. S. Liu, Y. Ou, X. Z. Liu, L. Gu, Y. Zhang, *Nat. Commun.* **2017**, 8, 15881.

[23]   Y. Wang, L. Qi, L. Shen, Y. H. Wu, *J. Appl. Phys.* **2016**, 119, 154301.

[24]   H. V. Han, A. Y. Lu, L. S. Lu, J. K. Huang, H. N. Li, C. L. Hsu, Y. C. Lin, M. H. Chiu, K. Suenaga, C. W. Chu, H. C. Kuo, W. H. Chang, L. J. Li, Y. M. Shi, *ACS Nano* **2016**, 10, 1454.

[25]   M. Amani, D.-H. Lien, D. Kiriya, J. Xiao, A. Azcatl, J. Noh, S. R. Madhvapathy, R. Addou, K. C. Santosh, M. Dubey, K. Cho, R. M. Wallace, S.-C. Lee, J.-H. He, J. W. Ager, X. Zhang, E. Yablonovitch, A. Javey, *Science* **2015**, 350, 1065.

[26]   S. Roy, W. Choi, S. Jeon, D. H. Kim, H. Kim, S. J. Yun, Y. Lee, J. Lee, Y. M. Kim, J. Kim, *Nano Lett.* **2018**, 18, 4523.

[27]   H.-V. Han, A.-Y. Lu, L.-S. Lu, J.-K. Huang, H. Li, C.-L. Hsu, Y.-C. Lin, M.-H. Chiu, K. Suenaga, C.-W. Chu, H.-C. Kuo, W.-H. Chang, L.-J. Li, Y. Shi, *ACS Nano* **2016**, 10, 1454.

[28]   H. Li, C. Tsai, A. Koh, L. Cai, A. W. Contryman, A. H. Fragapane, J. Zhao, H. Han, H. C. Manoharan, F. Abild-Pedersen, J. K. Nørskov, X. Zheng, *Nat. Mater.* **2015**, 15, 48.

[29]   S. Bhattacharjee, K. L. Ganapathi, D. N. Nath, N. Bhat, *IEEE Trans. Electron Devices* **2016**, 63, 2556.

[30]   A. Allain, J. H. Kang, K. Banerjee, A. Kis, *Nat. Mater.* **2015**, 14, 1195.

[31]   S. Choi, Z. Shaolin, W. Yang, *J Korean Phys Soc* **2014**, 64, 1550.

[32]   J. Peto, T. Ollar, P. Vancso, Z. I. Popov, G. Z. Magda, G. Dobrik, C. Y. Hwang, P. B. Sorokin, L. Tapaszto, *Nat. Chem.* **2018**, 10, 1246.

[33]   F. Giannazzo, G. Fisichella, A. Piazza, S. Di Franco, G. Greco, S. Agnello, F. Roccaforte, *Phys Status Solidi-R* **2016**, 10, 797.

[34]   L. Qi, Y. Wang, L. Shen, Y. Wu, *Appl. Phys. Lett.* **2016**, 108, 063103.

[35]   W. Zhang, J.-K. Huang, C.-H. Chen, Y.-H. Chang, Y.-J. Cheng, L.-J. Li, *Adv. Mater.* **2013**, 25, 3456.

[36]   D. Kufer, G. Konstantatos, *Nano Lett.* **2015**, 15, 7307.

[37]   B. K. Sarker, E. Cazalas, T. F. Chung, I. Childres, I. Jovanovic, Y. P. Chen, *Nat. Nanotechnol.* **2017**, 12, 668.

[38]   M. Buscema, D. J. Groenendijk, S. I. Blanter, G. A. Steele, H. S. J. van der Zant, A. Castellanos-Gomez, *Nano Lett.* **2014**, 14, 3347.

[39]   Q. H. Zhao, W. Wang, F. Carrascoso-Plana, W. Q. Jie, T. Wang, A. Castellanos-Gomez, R. Frisenda, *Mater. Horiz.* **2020**, 7, 252.

[40]   S. Pak, Y. Cho, J. Hong, J. Lee, S. Lee, B. Hou, G. H. An, Y. W. Lee, J. E. Jang, H. Im, S. M. Morris, J. I. Sohn, S. Cha, J. M. Kim, *ACS Appl. Mater. Interfaces* **2018**, 10, 38264.

[41]   Y. J. Fang, A. Armin, P. Meredith, J. S. Huang, *Nat. Photonics* **2019**, 13, 1.

[42]   G. Konstantatos, J. Clifford, L. Levina, E. H. Sargent, *Nat. Photonics* **2007**, 1, 531.

[43]   S. Pak, J. Lee, A. R. Jang, S. Kim, K.-H. Park, J. I. Sohn, S. Cha, *Adv. Funct. Mater.* **2020**, 30, 2002023.

[44]   J. Lee, S. Pak, P. Giraud, Y. W. Lee, Y. Cho, J. Hong, A. R. Jang, H. S. Chung, W. K. Hong, H. Jeong, H. Shin, L. G. Occhipinti, S. M. Morris, S. Cha, J. Sohn, J. Kim, *Adv. Mater.* **2017**, 29, 1702206.

[45]   J. Lee, S. Pak, Y. W. Lee, Y. Park, A. R. Jang, J. Hong, Y. Cho, B. Hou, S. Lee, H. Y. Jeong, H. S. Shin, S. M. Morris, S. Cha, J. I. Sohn, J. M. Kim, *ACS Nano* **2019**, 13, 13047.

[46]   G. Kresse, *J. Non-Cryst. Solids* **1995**, 193, 222.

[47]   G. Kresse, J. Furthmuller, *Phys. Rev. B* **1996**, 54, 11169.

[48]   J. P. Perdew, K. Burke, M. Ernzerhof, *Phys. Rev. Lett.* **1996**, 77, 3865.

[49]   J. Klimes, D. R. Bowler, A. Michaelides, *J Phys-Condens Mat* **2010**, 22, 022201.

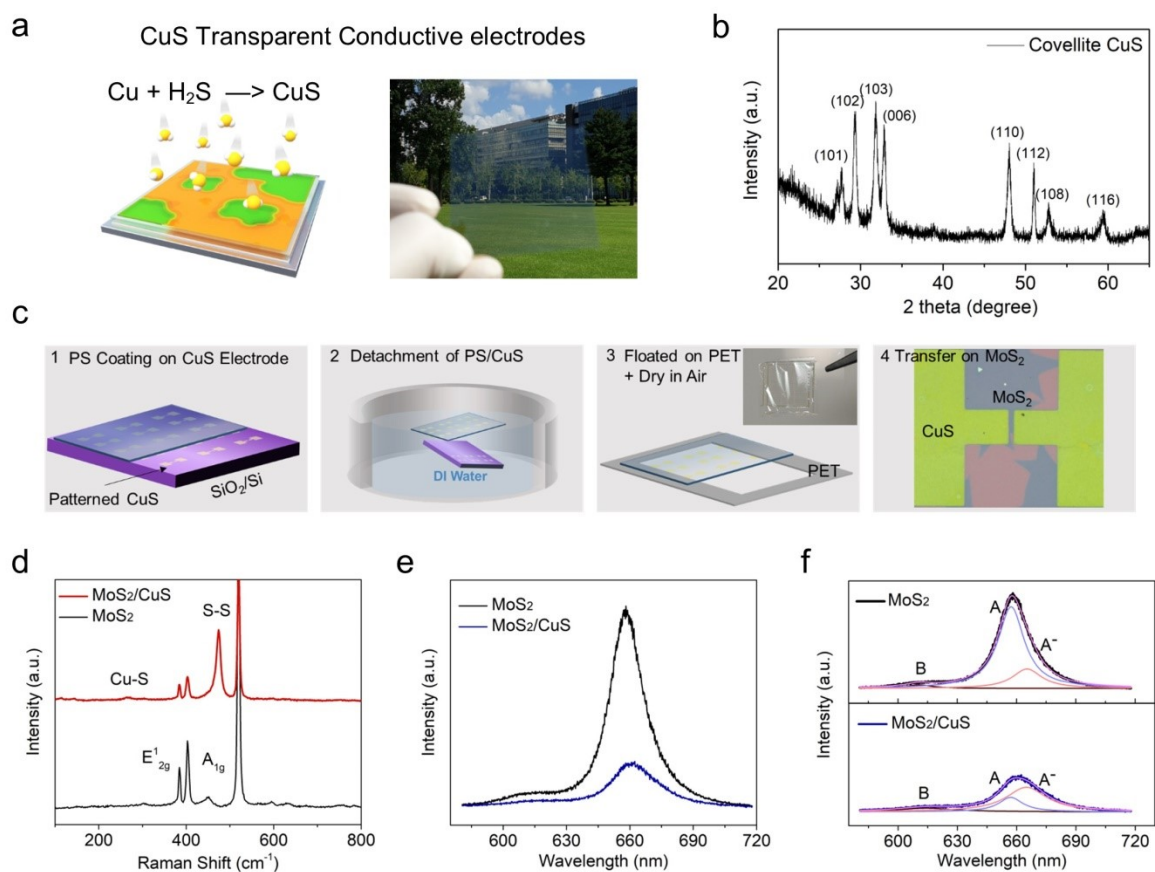[50]   P. E. Blochl, *Phys. Rev. B* **1994**, 50, 17953.

Author Manuscript

Figure 1. Synthesis and characterization of CuS and MoS$_2$/CuS hybrid structure. a) A schematic illustration and optical image of the CuS film synthesized using H$_2$S gas and Cu film b) X-ray diffraction pattern of CuS nanosheet. c) Fabrication procedures of MoS$_2$/CuS hybrid structure using polymer-assited transfer method. d) Raman and e) photoluminescence spectrum of MoS$_2$ and MoS$_2$/CuS hybrid structure. f) Deconvolution of the PL spectra to identify the relative contribution from trions (A$^-$) and exciton (A) by fitting with Lorentzian curves.
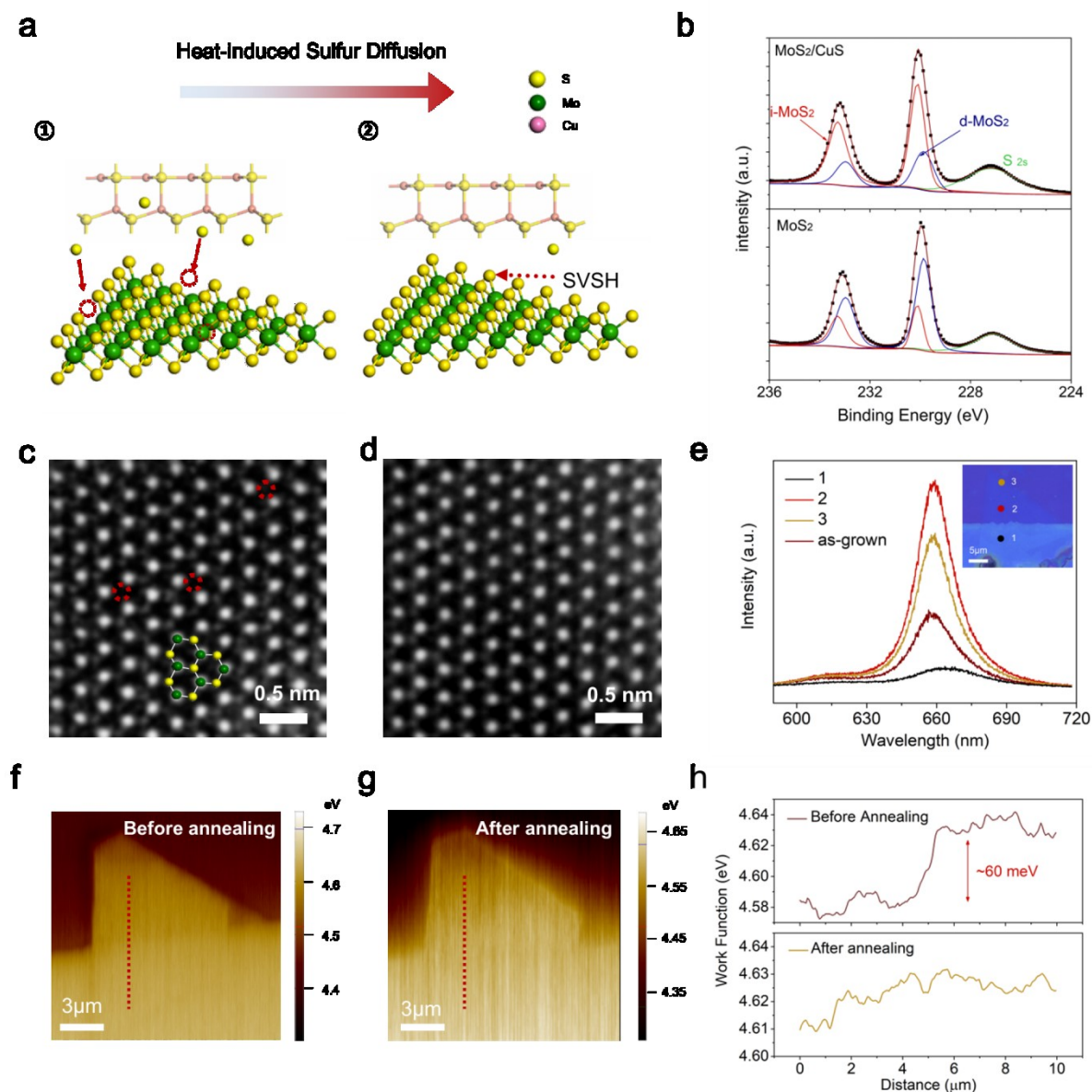
Figure 2. Sulfur-vacancy self-healing mechanism in the MoS_2/CuS hybrid structure. a) A schematic illustration of the annealing-induced self-healing of sulfur vacancies in MoS_2. b) X-ray photoelectron spectroscopy measurment of Mo 3d orbital in MoS_2 and MoS_2/CuS structure. ADF-STEM images of c) pristine MoS_2 and d) the self-healed MoS_2. e) PL spectrum taken from the points in the optical image (inst). f,g) Kelvin probe force microscopy two-dimensional mapping image of the MoS_2/CuS hybrid structure. h) KPFM line profile taken from the images in f,g)

22
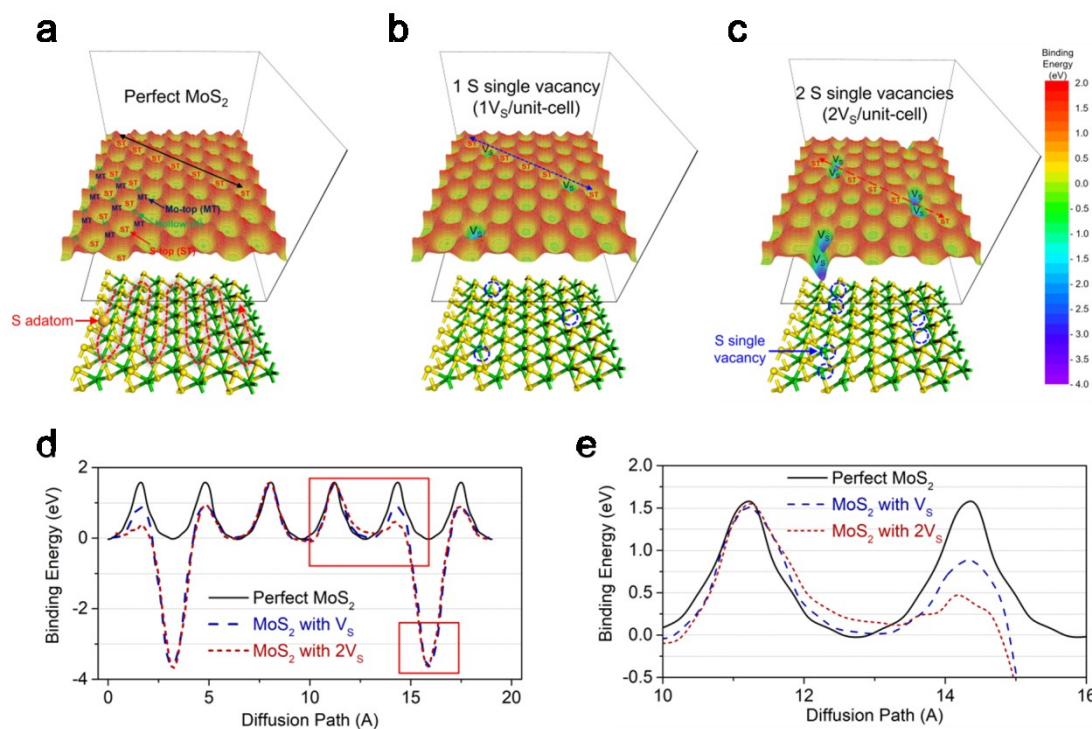
Figure 3. Binding energy surfaces (BESs) of a sulfur adatom on perfect and defective MoS_2 surfaces. BESs of a sulfur adatom placed in different positions (upper) and optimized atomic surface structures (lower) on a) perfect MoS_2, b) MoS_2 with sulfur single vacancy, c) MoS_2 with neighboring sulfur vacancies. The yellow and green spheres represent sulfur and molybdenum atoms, respectively. As displayed by the wavy red arrows in the lower figure of a), BESs were calculated by moving the position of a sulfur adatom on the perfect and defective MoS_2 surfaces. The blue circles in the lower figures of b) and c) imply the locations of the sulfur single vacancies. d) Energy barrier profiles for proposed surface diffusion paths (double-headed arrows in a-c) of a sulfur adatom. e) Encircled view of energy barrier profile

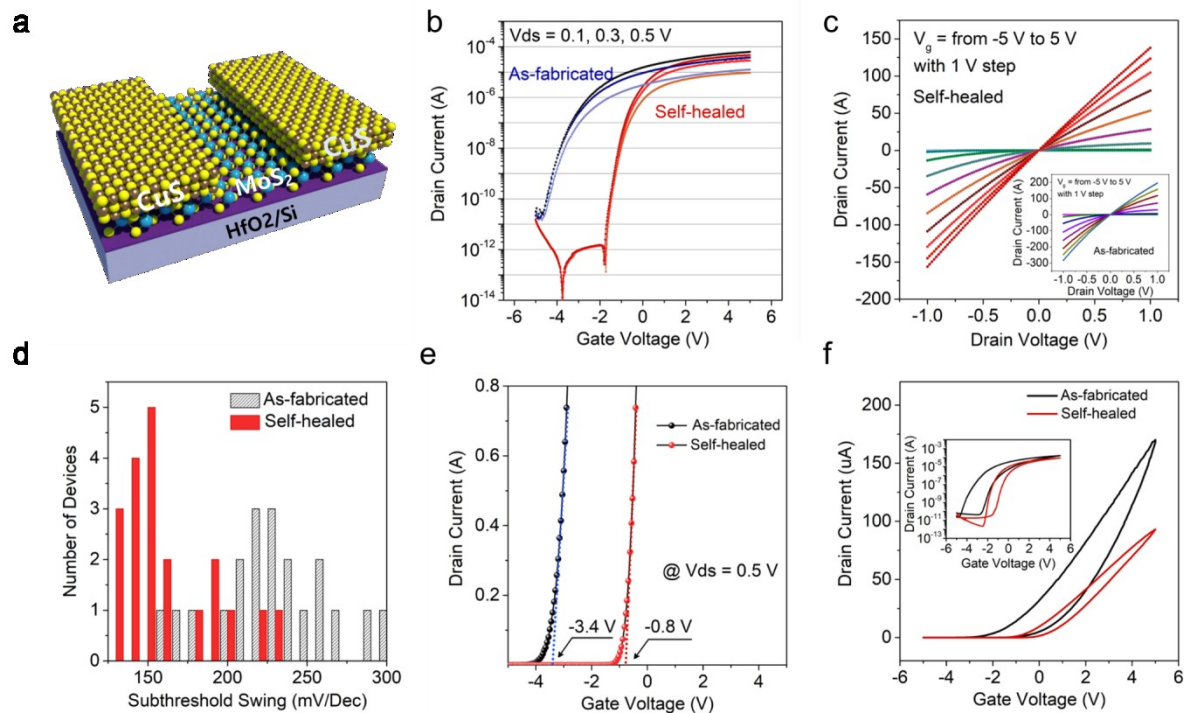corresponding to the hollow rectangular part in figure of d).

Figure 4. The MoS$_2$/CuS Transistor. a) Schematic illustration of the MoS$_2$/CuS transistor. b) Transfer curves at 0.1 V – 0.5 V source drain bias and c) output curves at different gate voltages (-5 to +5 V) of the as-fabricated and self-healed devices. Change in d) subthreshold swing values, e) threshold voltages, and f) hysteresis chracteristics after mild thermal annealing to induce self-healing in MoS$_2$.
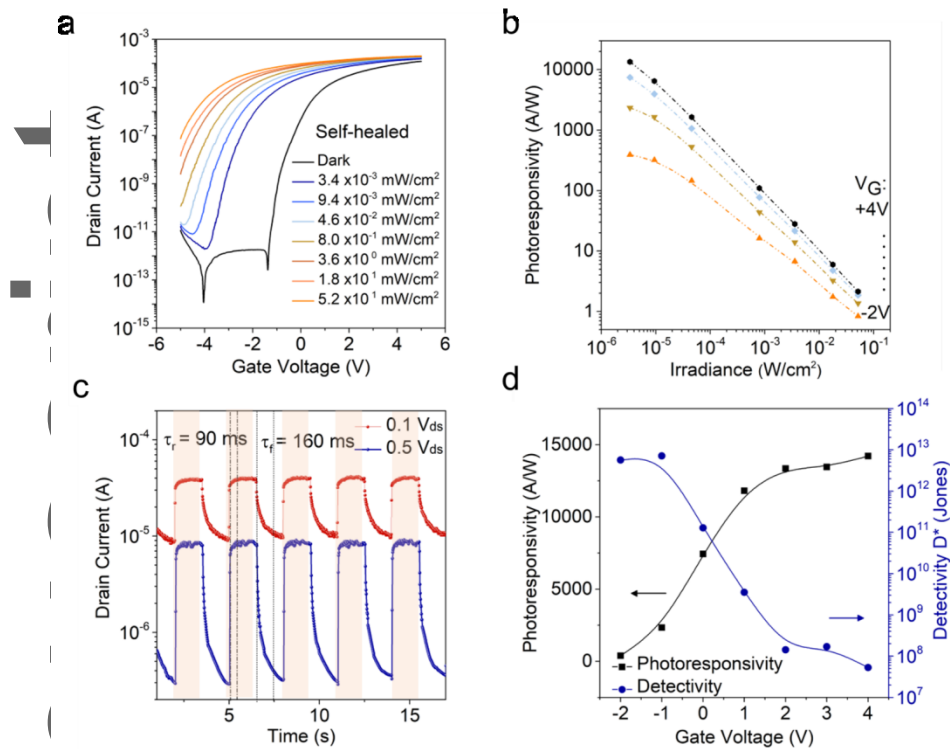
Figure 5. Phototransistor peformance of the self-healed MoS_2/CuS Phototransistor. a) Measurements of drain current as a function of gate voltages under different incident laser power densities (dark to 52 mW/cm^2). b) Photoresponsivity as a functino of incident laser power densities at differenet gate voltages (-2 to +4 V). c) Temporal response of photocurrent at drain voltages of 0.1 V and 0.5 V. d) Photoresponsivity (primary-axis) and detectivity (secondary-axis) as a function of gate voltages.

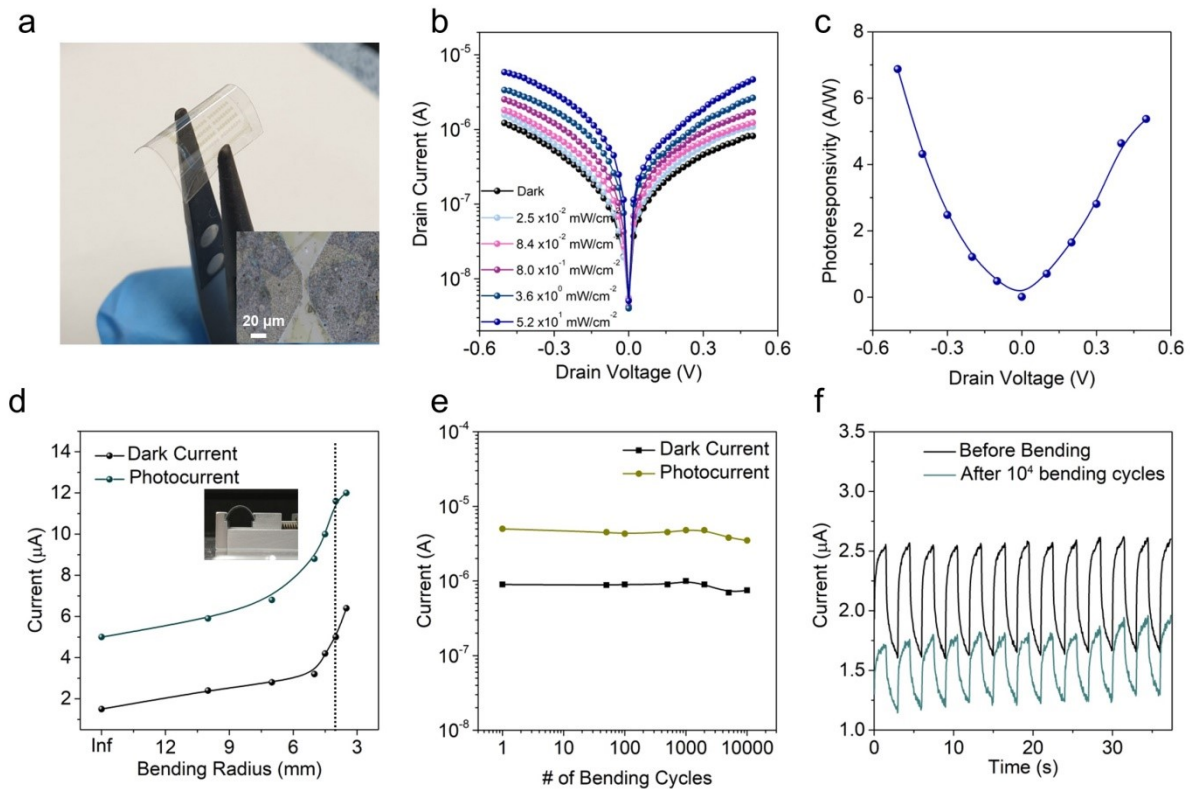**Figure 6**. Flexible MoS$_2$/CuS Photodetector. a) Optical image of the two-terminal MoS$_2$/CuS flexible device. b) The *IV*-curves of the MoS$_2$/CuS photodetector at varying illumination intensities. c) Photoresponsisivty as a function of applied drain voltages. The change in dark current and photocurrent measured with respective to d) bending radius and e) bending cycles. f) Temporal photocurrent measurement after 10^4 bending cycles.
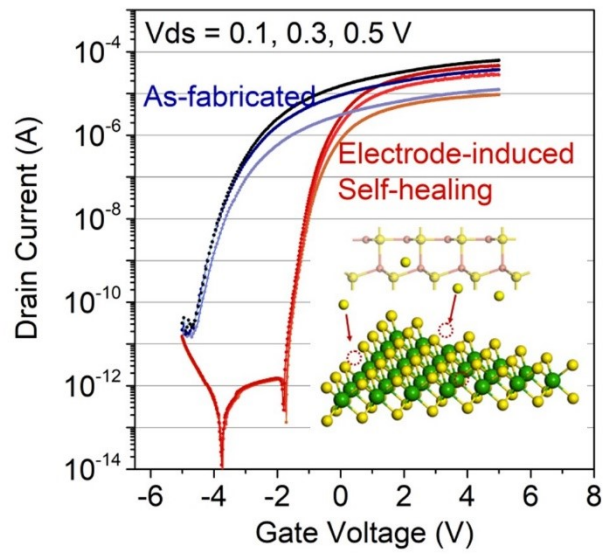
A novel sulfide electrode system allows sulfur-vacancy self-healing in 2D MoS_2. Ultrathin CuS electrode heals defects in MoS_2 channel spontaneously upon mild thermal annealing. The self-healed CuS/MoS_2 transistors and phototransistors show impressive device performance.